



Density-mediated spin correlations drive edge-to-bulk flow transition in active chiral matterAlexander P. Petroff , Christopher Whittington , and Arshad Kudrolli
Department of Physics, Clark University, Worcester, Massachusetts 01610, USA (Received 12 January 2023; revised 13 April 2023; accepted 23 June 2023; published 31 July 2023)

We demonstrate that edge currents develop in active chiral matter due to boundary shielding over a wide range of densities corresponding to a gas, fluid, and crystal. The system is composed of spinning disk-shaped grains with chirally arranged tilted legs confined in a circular vibrating chamber. The edge currents are shown to increasingly drive circulating bulk flows with area fraction as percolating clusters develop due to increasing spin-coupling between neighbors mediated by frictional contacts. Edge currents are observed even in the dilute limit. While, at low area fraction, the average flux vanishes except within a distance that is of the order of a particle diameter of the boundary, the penetration depth grows with increasing area fraction until a solid-body rotation is achieved corresponding to the highest packing, where the particles are fully caged with hexagonal order and spin in phase with the entire packing. A coarse-grained model, based on the increased collisional interlocking of the particles with area fraction and the emergence of order, captures the observed flow fields.

DOI: [10.1103/PhysRevE.108.014609](https://doi.org/10.1103/PhysRevE.108.014609)**I. INTRODUCTION**

Chiral active matter is composed of particles or organisms that intrinsically spin [1–6]. These materials are naturally out of equilibrium; energy and rotation are constantly supplied to the system on the scale of the particle, and dissipated by the global motion of the particles. The intrinsic rotation of each particle causes colliding particles to rotate about one another in a preferred direction. Consequently, locally increasing particle density also increases the local vorticity. The corresponding rheology of the chiral material is described by a dissipationless odd viscosity and odd elasticity [7,8]. The study of these systems gives insight into nonequilibrium pattern formation [9,10], may be relevant for the ecology of certain organisms [11,12], and aids the design of robots that couple translation to rotational modes [13,14].

Collections of chiral grains moving on a vibrated substrate, as in Fig. 1, provide an avenue by which to reach a deeper understanding of how particle rotation at an individual level can manifest itself collectively [1,15]. While collections of granular rods can self-assemble to form chiral structures which spin collectively [16], particles with tilted legs and bumpy sides, which promote frictional particle-particle interactions, have been demonstrated to spin, self-organize, and give rise to further collective motion [17–19]. However, many simple questions on the effect of particle concentration and differences on bulk versus boundary interactions remain unanswered. In vibro-fluidized granular systems, interactions occur only during contact and present the opportunity to investigate density effects over a wide range of area fractions, in contrast to systems in which secondary flows in the interstitial medium can give rise to attraction and other system-specific effects [11,20].

Here we examine the increasing effect of particle-particle density and spin correlations on the global flow in a monolayer of chiral active matter as their area fraction ϕ increases from that of a gas to a crystal. Past work, using similar ex-

perimental designs [17–19,21], have exclusively studied the dynamics of active chiral particles at relatively high area fractions, above ≈ 0.3 . Consequently, these experiments give little insight into how the edge current emerges and changes across the phases of chiral matter. To better understand the onset of global motion and systematic variation of the edge current across phases of active chiral matter, we measure the translational and rotational motion of particles as the area fraction increases from 0.078 to 0.746, which is the densest packing that could be practically achieved in our experiment. A coarse-grained model captures the systematic variation of the translational motion of particles across all area fractions examined. However, neither this model nor existing continuum theories predict the variation of particle angular velocity across the phases.

II. MATERIALS AND METHODS**A. Particle design and fabrication**

A schematic of the chiral particles used in our study is shown in Fig. 1(a). The particles are designed specifically to achieve two tasks: each particle is to spin on average in a desired direction, and each particle should be able to interact with other particles and exchange angular momentum. The particles are composed of a solid gear cap with outer radius $r_0 = 0.6$ cm with mass $m = 0.28$ g and moment of inertia $I = 0.04$ g cm². The seven slanted legs (length 3.3 mm, width 0.8 mm, angle 30°) are arranged in a circular pattern beneath the circular cap (height 2 mm, diameter 10 mm). Because the legs are slanted, striking the particle from below causes it to spin as it accelerates upwards off the plate [22]. Grain interactions are augmented using 25 triangular gear spokes (spoke length 1 mm) that can couple grains that are in contact with each other. To ensure that these particles are nearly identical, they are fabricated using a Formlabs 3D printer with a clear photopolymer resin. A white sticker is centered on the top of each grain to assist with tracking position; a black circle is

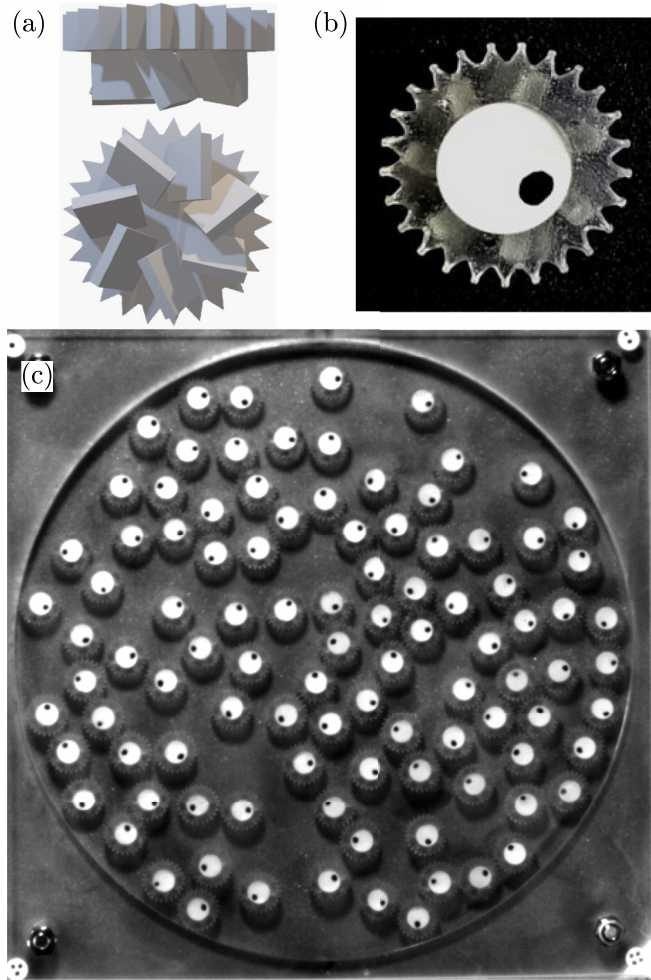


FIG. 1. Chiral particles are confined to a quasi-two-dimensional circular chamber. (a) A schematic of the chiral matter design viewed from the side and bottom. (b) A top view of a 3D-printed chiral particle. A white sticker with a black marker is added to find its location and spin rate. (c) Top view image of chiral particles in the circular chamber. The chiral particle monolayer sits atop the sandblasted aluminum plate and is confined by a clear acrylic lid.

drawn slightly off-center to assist with tracking the individual rotation as shown in Fig. 1(b).

B. Container and vibration system

Particles are confined within a quasi-two-dimensional cylindrical chamber of radius $R_c = 8.75$ cm that oscillates vertically with frequency $f = 60$ Hz and amplitude $A = 0.17$ mm. We vary the number of particles N_p from 20 to 191. These particles are placed in a quasi-two dimensional chamber which is connected via a linear bearing to an electromagnetic shaker (Labworks Inc. Model PA-141) connected to an Agilent waveform generator [16]. The linear bearing ensures that the vibrations are purely vertical as tested with an accelerometer to within 1%. This chamber is composed of an aluminum base that is bolted to clear acrylic walls and a cap. The aluminum base was lightly sandblasted to excite the diffusive motion of the particles and dyed black to contrast with the particles. The height of the chamber, 6.35 mm is

slightly greater than the particle height, which is 5 mm. The chamber is vibrated at 60 Hz. The amplitude is adjusted such that the maximum of the measured acceleration is 2.5-times the Earth's gravitational acceleration.

A PixelLink camera above the chamber records the two-dimensional motion of the particles. An example is shown in Fig. 1(c). Images are acquired at 50 ms intervals over 10-min time intervals.

C. Particle tracking

We begin by describing the tracking of the particles. The white 6 mm sticker placed on the center of each particle are sharply contrasted with the opaque particles and dark substrate. Knowing the radius of each sticker allows one to quickly identify their centers by applying a Circular Hough Transform. The pairwise distances between particles in sequential frames are then computed. The assignment of instantaneous locations to particle tracks is performed using Munkres' Assignment Algorithm. In the rare circumstances that a particle is not found in a particular frame, its position is interpolated from its positions immediately before and after the missing frame. In a typical experiment, fewer than 0.06% of particle positions are interpolated. At the lowest area fractions examined, where the particle velocity is greatest, as many as 1.6% of positions are interpolated.

A similar method is used to track particle orientation. A small black spot is drawn on each sticker at a point about halfway between its center and edge. After the center of the particle is found, the mean intensity of the sticker is radially averaged to give the mean intensity as a function of orientation about the center of the particle. The dark spot appears as a minimum in the intensity at a particular angle. Fitting a parabola to the minimum allows one to track the spot with subpixel resolution. These measurements are assembled into trajectories, which show the change in particle orientation from the beginning of the experiment.

To move to a reference frame that rotates with the collective motion of the particles (as in supplementary videos SV2 and SV3), we first calculate the velocity \mathbf{v} of each particle in the laboratory frame. We then find the average angular velocity of the average flow as $\Omega = \langle \mathbf{v} \times (\mathbf{r} \times \hat{\mathbf{z}}) / r^2 \rangle$, where \mathbf{r} is the vector from the center of the chamber to a particular particle, and $\hat{\mathbf{z}}$ is normal to the vibrating plate. We then change coordinates to one that rotates with the instantaneous angular velocity Ω .

D. Kinetics of isolated particles

Isolated particles are found to spin counterclockwise on average when viewed from above with a mean angular velocity of $\omega_0 = 7.61 \pm 0.01$ s⁻¹. Particles diffuse with translational diffusion coefficient $D = 0.134 \pm 0.07$ cm²/s and rotational diffusion coefficient $D_r = 3.4 \pm 0.4$ rad²/s.

III. RESULTS

A. Variation of packing geometry and global flow with packing fraction

Figure 2 shows representative snapshots of the system corresponding to gas, fluid, and crystal phases with increasing ϕ ,

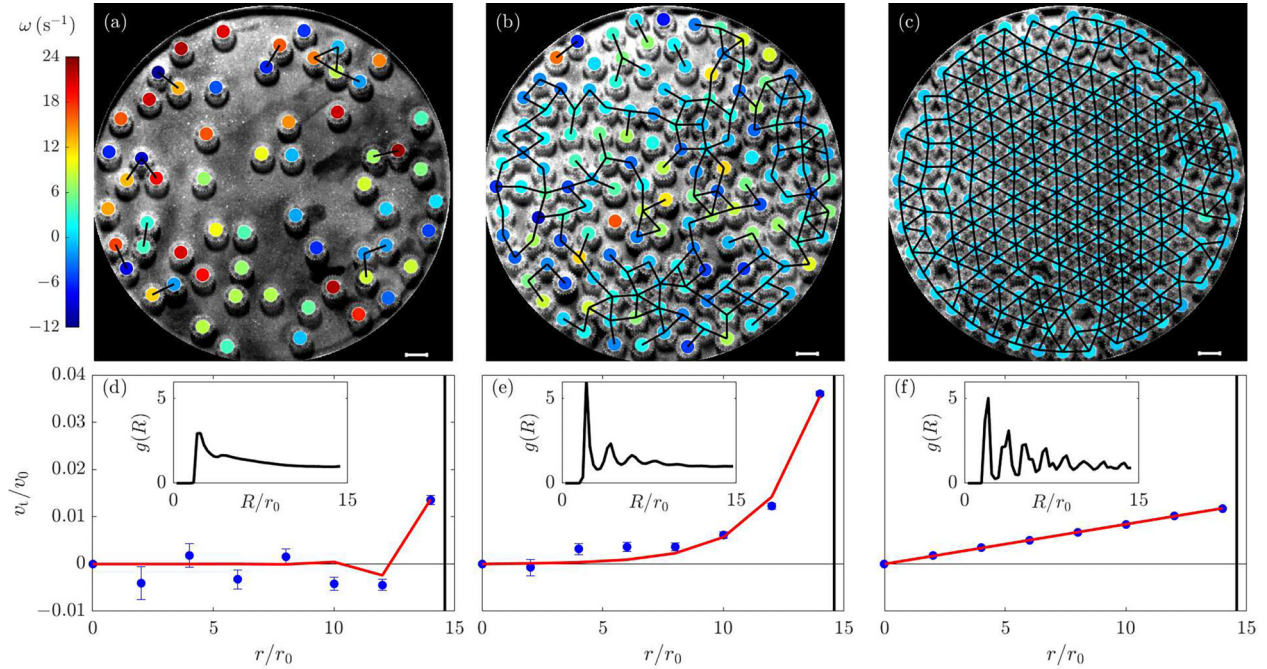


FIG. 2. The dynamics of a chiral material is examined across the phases of gas (left column), fluid (center), and crystal (right). Panel (a) shows the distribution and angular velocities (colored spots), and contact network (solid black lines) of 60 particles in a dilute gas ($\phi = 0.23$). The scale bar is 1 cm. Panels (b) and (c) show the corresponding particle locations, angular velocities, and contact networks in a fluid of 148 particles ($0.57 < \phi_{\text{hex}}$) and a crystal of 191 particles ($\phi = 0.74 > \phi_{\text{hex}}$), respectively. Note that the mean and variance of the angular velocities decrease with ϕ . The bottom row shows the radial velocity profile for the (d) gas, (e) fluid, and (f) crystal. Red lines are fits to the coarse-grained model [Eqs. (1)–(4)]. The insets show the pair correlation function $g(R)$. The location first peak, which is insensitive to ϕ , is found at a distance 1.08 ± 0.05 cm. This value is between inner (1 cm) and outer (1.2 cm) particle diameters.

and a corresponding video can be found in Supplemental Material video SV1 [23]. We have further superimposed the spin angular velocity ω on the tracked position of each particle. We observe that the system becomes increasingly ordered not only in the way the particles are arranged, but also in terms of their spin, with the highest ϕ showing hexagonal crystalline order and little variation in ω . We construct the contact network from instantaneous positions of the particles, taking two particles to be in contact if their center to center distance is less than $2.2r_0$, and is also shown in Figs. 2(a)–2(c). As ϕ is further increased, the contact network becomes ordered and the disordered fluid becomes a crystal.

To characterize the emergence of flow and its nature, we calculate the tangential velocity of each particle as it moves about the center of the chamber. Averaging these instantaneous measurements over 10-min trials, we find the steady-state velocity profile v_r as a function of distance r from the chamber center. The corresponding profiles are shown in Figs. 2(d)–2(f), nondimensionalized by the characteristic speed $v_0 = r_0\omega_0 = 4.6$ cm/s of an isolated particle’s edge. In all cases, particle speed is maximum within a particle diameter of the chamber wall, where they move with flux $j_{\text{edge}} = 2r_0v_r$. The overall collective rotation in the chamber is in the same direction as the individual particle spin, which implies that the flow is driven by particle-particle collisions rather than particle-boundary interactions [24]. The measured v_r of each data set obtained between $\phi = 0.078$ and 0.746 can be found in Fig. 9. Our results provide the first experimental investiga-

tion of flows driven by chirality as the density varies widely, corresponding to a chiral gas, fluid, and crystal states.

To quantify these transitions, we plot in Fig. 3(a) the six-fold orientational correlation function $Q_6(R) = \langle q_6(\mathbf{R})q_6^*(0) \rangle$, where $q_6(\mathbf{r}_k) = N_k^{-1} \sum_{j=1}^{N_k} e^{i6\theta_{k,j}}$, \mathbf{R} is the position vector (of magnitude R) between the centers of two particles, N_k is the number of particles that particle k contacts, \mathbf{r}_k is the position vector of the particle k from the center, and $\theta_{k,j}$ is the angle between particles k and j , which are in contact with one another. As shown in Fig. 3(b), particle orientation becomes correlated at a critical area fraction of $\phi_{\text{hex}} = 0.64$ over the scale of the chamber R_c and the hexagonal packing of particles becomes apparent as in Fig. 2(c). The pair-correlation function $g(R)$, which describes the density variation as a function of distance R from a particle, is shown in the insets of Figs. 2(d), 2(e), and 2(f). They are observed to be consistent with those of a gas, fluid and crystalline solid, respectively, with the appearance of peaks growing at $R = 2r_0$, $2\sqrt{3}r_0$, and $4r_0$ corresponding to a hexagonal lattice. (The measured pair correlation function can be found in Fig. 10 for each experiment.) The small secondary peak is absent at the lowest area fraction examined.

Because colliding particles tend to rotate about one another, collisions transfer angular momentum from the individual rotation of particles to the global rotation about the chamber. As the contact network grows and spatial correlations increase with ϕ , the average spin angular velocity $\langle \omega \rangle$ and its root-mean fluctuations decreases as shown in Fig. 3(c). We measure the particles’ instantaneous two-dimensional

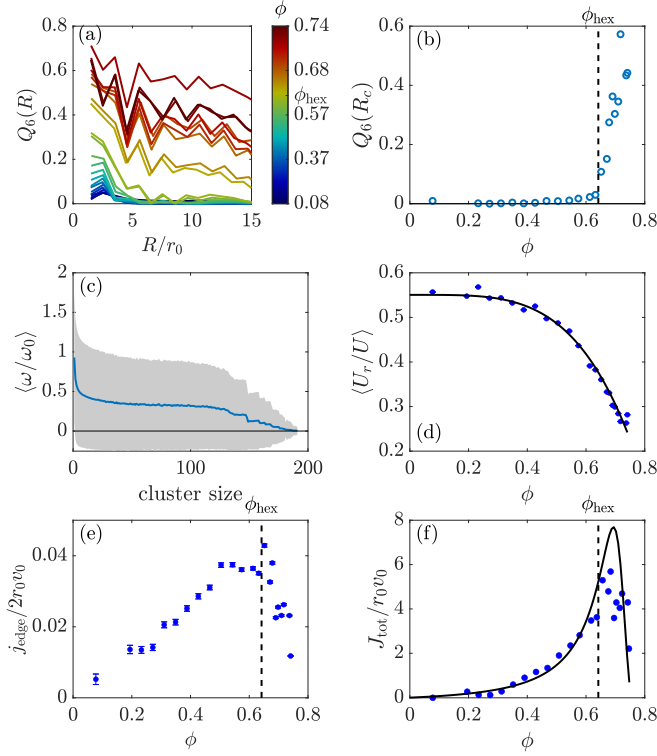


FIG. 3. Cluster geometry and particle motion vary systematically with area fraction. (a) The magnitude and correlation length of the orientation of particle contacts grows with area fraction. (b) The formation of a single rotating crystal is identified from the point at which $Q_6(R_c)$ increases discontinuously. (c) Average angular velocity particles (blue line) and the typical fluctuations (shaded region) decrease as the size of the contact network grows. (d) As area fraction increases, the rotational motion is slowed more quickly than translational components. The black line, shown as a guide to the eye, is $\langle U_r/U \rangle = 0.55 - 1.03\phi^4$. (e) The edge current j_{edge} is a nonmonotonic function of ϕ which changes abruptly at ϕ_{hex} . (f) The integrated particle flux J_{tot} is maximized at $\phi = 0.69$. The black line shows the predictions of Eqs. (1)–(4).

translational kinetic energy $U_t = \frac{1}{2}mv_{2D}^2$, where v_{2D} is the instantaneous translational speed of a particle, the rotational kinetic energy $U_r = \frac{1}{2}I\omega^2$, and the total measured energy $U = U_r + U_t$. As shown in Fig. 3(d), the partitioning of energy between translational and rotational motion $\langle U_r/U \rangle = 0.55$ in the gas phase, and decreases quartically with ϕ in the fluid phase. As the packing becomes crystalline—close to ϕ_{hex} —and ω of the particles locks in phase with the solid-body rotation, $\langle U_r/U \rangle$ becomes similar to $1/3$, the value predicted by the equipartition theorem.

In the dilute limit of a chiral gas, particle collisions are dominated by two-body interactions. Because the corotation of isotropically colliding particles generates no net flow, the velocity field vanishes in the interior of the chamber [21]. The presence of the chamber wall breaks this symmetry. Because a particle near the wall can only be struck from the chamber interior, the outer ring of particles slip over the chamber walls as they are pushed from the interior. Since this mechanism does not reference a particular ϕ , one may expect an edge current even at vanishing densities. Edge

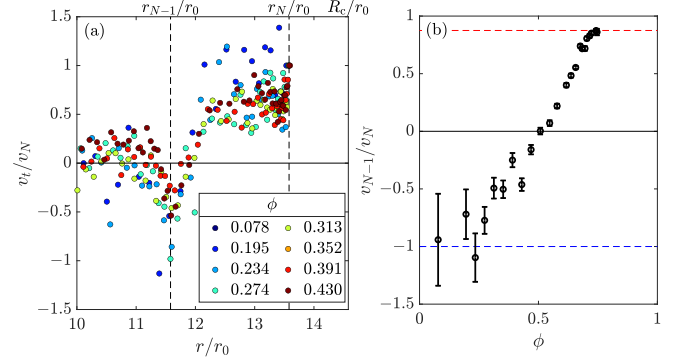


FIG. 4. Retrograde motion is observed in particles centered a distance $r_{N-1} = R_c - 3r_0$. (a) The tangential velocity profile is shown on a much finer scale than in Figs. 2(d)–2(f) to highlight the retrograde. (b) The ratio of tangential velocities of particles in the two outermost annuli increases monotonically from -1 , correspond to elastic two-body collisions (blue dashed line), to $7/8$, which corresponds to solid-body rotation (red dashed line).

currents have been shown to develop in a numerical study of a dilute ($\phi \approx 0.12$) gas of driven rotors interacting with Yukawa potential [4]. Figure 3(e) shows that edge currents form at area fractions as low as 0.078 even in systems which interact sterically. We find that j_{edge} increases approximately linearly with ϕ , and j_{edge} apparently can extend to vanishing densities provided particle-particle collisions are present. The corresponding flux $J_{\text{tot}} = 2\pi \int \phi v_t r dr$ is shown in Fig. 3(f). Our experiments show that a thin edge current ($2r_0$ wide) is maintained by short-range particle-particle interactions in a dilute gas. Confinement induced packing structure has been shown numerically to give rise to oscillatory flows at intermediate ϕ , but were not clearly realized in their corresponding experiments [21].

Interestingly, we observe a clear signature of oscillatory flow for $\phi < 0.5$ with a weak counterclockwise flow for $11 < r/r_0 < 12$ as a reaction to the clockwise edge current. To highlight this slight retrograde motion, Fig. 4(a) shows the average tangential velocity v_t of dilute particles near the outer boundary of the chamber. Rescaling these measurements by the speed v_N of the outermost ring of particles collapses the velocity profile onto a similar form. These profiles show retrograde motion $v_{N-1} < 0$ of particles at a distance $r_{N-1} = R_c - 3r_0$ from the center of the chamber, which correspond to the annulus of particles that contact the outermost ring of particles. As the area fraction of particles increases, the ratio v_{N-1}/v_N increases monotonically and retrograde motion vanishes at an area fraction of 0.5. This ratio is bounded from below by $v_{N-1}/v_N > -1$, which corresponds to elastic two-particle collisions. The upper bound $v_{N-1}/v_N < (N-1)/N$ corresponding to solid-body rotation. The chamber studied here fits $N = 8$ concentric annuli of particles. Note that the retrograde motion is attenuated in Figs. 2(d)–2(f), where the tangential velocity is averaged over the width of a particle rather than evaluated at the midpoints of concentric annuli.

As ϕ rises, the edge current and associated flux, initially grows and extends through the system [Figs. 3(e) and 3(f)]. We observe that a disordered contact network [Fig. 2(b)] maintains flow in the bulk, and thus conclude that bulk flow

does not require the percolation of solid-like regions (see Appendix B). Rather, around an area fraction of 0.5, the contact network spans the chamber and the outermost particles cannot move independently of those in the interior. However, the loose contact network permits the relative motion of particles. As the outermost shell of particles is pushed around the exterior of the chamber, it drags the loose network. In this regime, velocity gradients begin to extend through the entire material [Fig. 2(e)].

Finally, in the dense regime, $\phi > \phi_{\text{hex}} = 0.64$, steric interactions arrest the relative motion of particles, velocity gradients are suppressed, and particles cease to rotate independently of the lattice except near defects. The amplitude of the edge current decays quickly with particle concentration [Fig. 3(e)] and the crystal moves as a solid body [Fig. 2(f)]. Interestingly, solid-body rotation is maintained even as system scale dislocations form (see Supplemental Material video SV2 [23]). In the crystalline limit, particles rotate in phase with the solid-body rotation except near topological defects (see Supplemental Material video SV3 [23]).

B. Coarse-grained model

To understand the variation in the particle flux with increasing area fraction, we develop a coarse-grained model. According to this model, particles are confined by steric interactions to move around the center of the chamber along concentric circular paths, which we call lanes. Collisions between particles transfers momentum between neighboring lanes and particles are slowed as they move relative to the chamber floor. The simple geometry assumed by this coarse-graining scheme makes it possible to calculate torque balance on each particle and on each lane, which is sufficient to determine the steady-state translational and angular velocities of each particle.

We first motivate this coarse-graining scheme, which respects the finite size of particles and the emergent crystalline structure, from the measured trajectories of particles. At particle concentrations above $\phi > \phi_{\text{hex}}$, particles rotate about the chamber in eight concentric lanes [Fig. 5(a)]. The outermost lane—at a distance of one particle radius from the outer wall—is apparent even at the lowest concentration examined. Multiple lanes become apparent around $\phi \approx 0.5$ at which contact networks begin to span the system [Fig. 5(a)]. We coarse-grain this system in a manner in which each lane—having a width of one particle diameter and the outermost lane is centered one particle radius from the outer wall—is densely occupied with the average particle concentration as illustrated Fig. 5(b).

Consider the torque balance on particles in the i th lane from the center with velocity v_i and spin angular velocity ω_i , where $i < N$ and $N \approx R_c/(2r_0)$ is the number of lanes that fit in the experiment. The rotation of these particles is slowed at rate α_p if the speed of its edge is faster than those of its neighbors. The corresponding nondimensionalized torque balance on the particles, as derived in Appendix A, is

$$\omega_i + \frac{\alpha_p}{\alpha_b} (v_{i-1} - v_{i+1} + \omega_{i-1} + 4\omega_i + \omega_{i+1}) = 1, \quad (1)$$

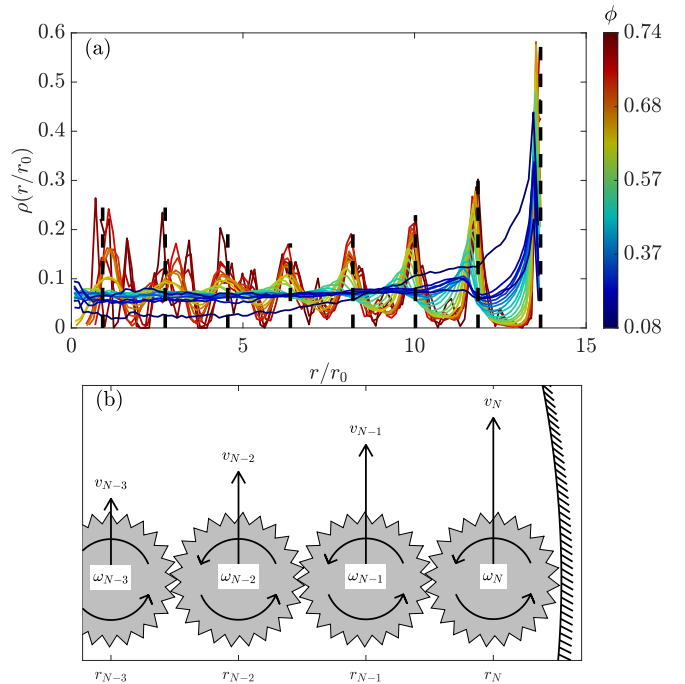


FIG. 5. Particles rotate about the center of the chamber in concentric lanes. Lanes form from the outer boundary and grow inwards with increasing ϕ . (a) The probability density function ρ for particle density for all experiments analyzed is shown. The dashed lines show the expected locations of lanes. (b) A schematic of particles interacting between lanes. Each particle moves in a circular path at velocity v_i and rotates about its axis at angular velocity ω_i .

where α_b is the rate that particle rotation is slowed by the bottom of the chamber. In the outermost lane, particle rotation is only slowed by collisions from the interior, within its lane, and the bottom of the chamber. The boundary condition on particle rotation at the wall is

$$\omega_N + \frac{\alpha_p}{\alpha_b} (v_{N-1} - v_N + \omega_{N-1} + 3\omega_N) = 1. \quad (2)$$

We assume that ω is smooth and continuous near $r = 0$.

Similarly, v_i is slowed at rate β_p if a particle's edges move more quickly than the edges it contacts. The corresponding torque balance on lane $i < N$ requires

$$v_i = \frac{\beta_p}{\beta_b} (v_{i-1} - 2v_i + v_{i+1} - \omega_{i+1} + \omega_{i-1}), \quad (3)$$

where β_b is the rate that the translational velocity is slowed by the bottom of the chamber. Again, the outermost particles are only affected by particles in the lane centered at r_{N-1} . The corresponding boundary condition is

$$v_N = \frac{\beta_p}{\beta_b} (v_{N-1} - v_N + \omega_{N-1} + \omega_N). \quad (4)$$

The boundary condition at the center of the chamber requires the angular velocity $\Omega = v_i/r$ to be smooth and continuous.

In the continuum limit $R_c \gg r_0$, Eqs. (1)–(4) predict an exponentially decaying edge current with penetration depth $\lambda_c = r_0 \sqrt{[\beta_p(2\alpha + 1)]/(3\alpha + 1)}/\beta_b$. In this limit, as α and β grow, the penetration depth grows from the particle scale [as in Fig. 2(d)] to scales much larger than the system size, which

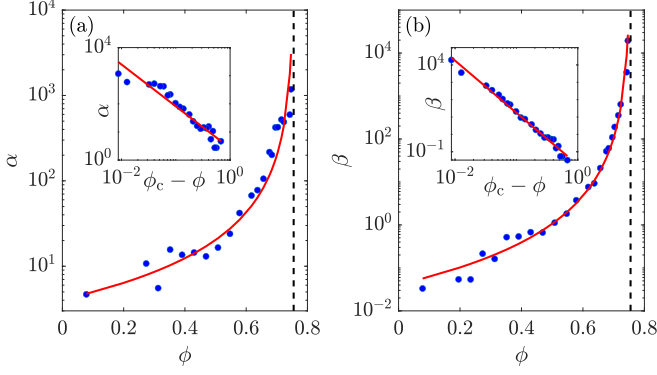


FIG. 6. The rates at which particle (a) angular velocity and (b) translational velocity relax to the speeds of the neighboring edges both diverge at the maximum area density. The red lines are fits to power laws. The insets show the same data on logarithmically scaled axes.

corresponds to solid-body rotation [see Fig. 2(f)]. This result is similar in form to the prediction for continuum models of active chiral materials [25] in which the penetration depth is $\sqrt{(\eta + \eta_o)/\beta_b}$, where η is the shear viscosity and η_o is the odd viscosity.

C. Comparison of experiment and theory

Equations (1)–(4) uniquely determine the tangential velocity and the angular velocity of particles in each lane. We fit the dimensionless relaxation rates $\alpha = \alpha_p/\alpha_b$ and $\beta = \beta_p/\beta_b$ to match the measured velocity profile. Three representative fits are shown in Figs. 2(d)–2(f), and all the trials are shown in Fig. 9. Remarkably, this model reproduces the velocity profile even in the dilute regime and correctly predicts the slight retrograde motion in the $N - 1$ lane [Figs. 2(d) and 4].

Intuitively, the relaxation rates α and β should increase with particle density as increasing the number of collisions similarly increases the rate particles are slowed by their neighbors. As shown in Fig. 6, α and β increase faster than exponentially with area fraction. These trends are well fit by power law divergences $\alpha(\phi) = \alpha_0(\phi_c - \phi)^{-\gamma/2}$ and $\beta(\phi) = \beta_0(\phi_c - \phi)^{-\gamma}$, where $\alpha_0 = 1.53$, $\beta_0 = 0.17$, $\gamma = 3$, and $\phi_c = 0.76$.

Figure 3(f) shows that the particle flux predicted by the power law divergences of α and β approximates the measured flux reasonably well. The predicted flux is not monotonic [26] and is maximized at $\phi \approx 0.69$ and is similar to the value $\phi_s = 0.711$ at which a large two-dimensional lattice of hard spheres transitions from diffusive behavior to caging, as discussed by Reis *et al.* [27]. The slightly lower value could result from the difference in particle shapes and finite size effects. This similarity suggests that flux is maximized when the rate of particles collisions is maximized before the relative motion of particles is arrested.

At an area fraction of $\phi_c = 0.76$ the rate coefficients α and β diverge and the system is stationary. While this value is substantially less than the maximum area fraction $\pi\sqrt{3}/6 \approx 0.907$ of disks in an infinite plane, it is slightly greater than the densest packing that could be practically achieved (0.74). This values corresponds to 196 particles, five more than are

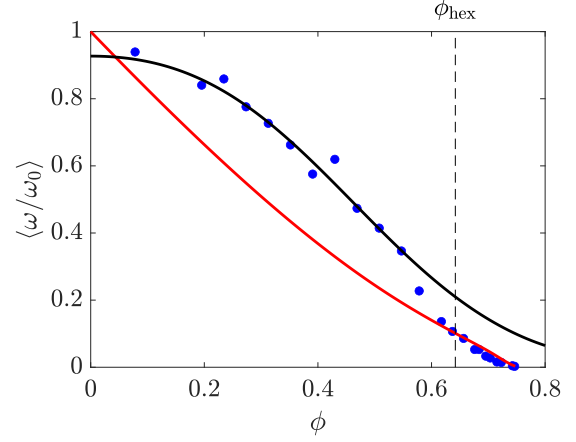


FIG. 7. The average angular velocity of particles (blue dots) decreases as the area fraction increases. The red line shows the predictions of Eqs. (1)–(4), which assumes a dense packing of particles. The black line shows a three parameter fit to the model of Liu *et al.* [21], which treats the material as a disordered fluid.

shown in Fig. 2(c). We conjecture that α and β diverge at the maximum packing fraction and the smaller value found here is due to the finite size of the chamber.

Finally, we compare the predictions of the coarse-grained model to the measured angular velocities of particles. The average angular velocities of particles decrease smoothly with increasing area fraction (see Fig. 7). The inferred rotation speed at vanishing area fraction is slightly less than ω_0 as a result of friction between particles and between particles and the chamber walls. The average angular velocities predicted by the power-law divergence of α and β systematically underestimate the actual angular velocity for two reasons. The first is because the best fit power-law divergences of α and β are nonzero at vanishing area fraction. Consequently, particles are predicted to rotate with angular velocity $\approx 0.1\omega_0$. Rescaling the predicted mean angular velocity by this factor gives the red line shown in Fig. 7. Although agreement is good for $\phi > \phi_{\text{hex}}$, the predictions of our coarse-grained model continue to underestimate the angular velocity at low density. For comparison, the black line shows a three parameter fit to a model proposed by Liu *et al.* [21], which relies on an expansion of the pair correlation function for a low densities fluid. The fit gives a good representation of angular velocity at low density but fails as expected at high densities.

IV. CONCLUSION

In conclusion, we have analyzed the evolution of edge current and bulk flow across three phases of active chiral matter. Edge currents are observed even at vanishing densities due to occasional particle collisions and shielding of particles at the boundaries. In the dilute limit ($\phi < 0.4$), particle-particle collisions generate a global flow that is confined within a narrow band within the width of a single particle of the chamber boundary. Both convection at low densities and the linear dependence is nonintuitive, and have not been anticipated. Only simulations [4] of particles with Yukawa interactions show edge currents similar to what we observe. Collisions between particles near the boundary and those in the interior

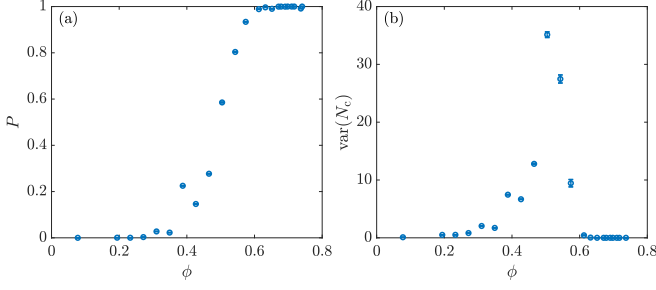


FIG. 8. The contact network percolates. (a) The weight P is the probability that a randomly selected particle is in a spanning network. It grows with area fraction. (b) Cluster sizes are most widely distributed at $\phi_{\text{perc}} \approx 0.5$. N_c is the number of particles in a nonspanning cluster.

produces slight retrograde motion in the bulk. This motion is suppressed at intermediate area fractions where steric interactions prevent the independent motion of particles. Upon the onset of system-scale orientational order, the edge current is quickly arrested and particles rotate as a solid body.

A coarse-grained model, which respects the emergent crystalline order and the finite particle size, accurately fits the measured velocity profile across these phases. These fits reveal that the rates α and β that particles are slowed by collisions with neighbors increase faster than exponentially with area fraction and appear to diverge at a value ϕ_c slightly greater than what could be practically achieved.

The comparison of this model to the measured motion of particles leaves open two questions which should be addressed by future work. First, it is unclear if α and β diverge at the maximum packing fraction, as we suspect, or if ϕ_c separates two distinct phases of chiral material. Increasing the size of chamber relative to the particle size would address this question. Next, the divergences of α and β are well fit by the relation $\alpha^2 \propto \beta$. We lack any physical model to explain this curious coincidence.

Finally, neither our coarse-grained model nor the continuum model of chiral fluids composed of particles similar to those studied here [21] is sufficient to understand particle rotation across the phases. While our coarse-grained model, which assumes a density of particles that is sufficient to maintain circular trajectories, fits that data well at high concentrations, it fails in the fluid regime. By contrast, the continuum model, which assumes a disorder fluid, fails for crystalline packings of particles. The experimental results presented here provide a strong test for any further theory to be developed to describe the fluid-solid transition of active chiral materials.

ACKNOWLEDGMENTS

We thank Trinh Huynh and Animesh Biswas for help with building experimental components and Jörn Dunkel for bringing Ref. [4] to our attention. This work was partially supported by NSF Grants No. DMR-2005090 and No. PHY-2042150.

APPENDIX A: DERIVATION OF THE COARSE-GRAINED MODEL

In this section we derive Eqs. (1)–(4) of the main text and discuss their fit to the measured velocity profile. According to

our model, a particle is accelerated and spun if its edge moves at a different speed than those of its neighbors. Particles in the i th lane are characterized by a velocity $v_i = r_i \Omega_i$, where Ω_i is the angular velocity of the lane about the center of the chamber, and composed of particles that rotate about their centers with angular velocity ω_i . The speed of a particle's outer edge is $v_i + \omega_i r_0$ and the speed of its inner edge is $v_i - \omega_i r_0$.

Each particle experiences a torque τ_b when it is struck by the vibrating plate, which causes it to rotate with an average angular velocity $\omega_0 = \tau_b / (I \alpha_b)$, where I is the moment of inertia and α_b is a rate coefficient. At steady state, this torque is balanced by friction with other particles and the bottom plate. The angular velocity of particle in the i th lane increases if its edges spin more slowly than those of its neighbors. Particles experience a torque from the interior lane of

$$\tau_- = -I \alpha_p [(v_{i-1} + \omega_{i-1} r_0) - (v_i - \omega_i r_0)] / r_0, \quad (\text{A1})$$

where α_p is a rate coefficient. The corresponding torque from the exterior lane is

$$\tau_+ = -I \alpha_p [(v_{i+1} - \omega_{i+1} r_0) - (v_i + \omega_i r_0)] / r_0. \quad (\text{A2})$$

A particle is also slowed by collisions within its lane, which exert a torque

$$\tau_0 = -2I \alpha_p \omega_i. \quad (\text{A3})$$

Friction with the base plate exerts a drag

$$\tau_D = -I \alpha_b \omega_i. \quad (\text{A4})$$

Torque balance on the particle requires $\tau_b + \tau_+ + \tau_- + \tau_0 + \tau_D = 0$, or equivalently

$$\begin{aligned} \alpha_p (v_{i-1} - v_{i+1} + r_0 \omega_{i-1} + 2r_0 \omega_i + r_0 \omega_{i+1}) + \alpha_b r_0 \omega_i \\ = \alpha_b r_0 \omega_0. \end{aligned} \quad (\text{A5})$$

After nondimensionalizing v_i by $r_0 \omega_0$ and ω_i by ω_0 , this analysis yields Eq. (1) of the main text. At the outer boundary, where $\tau_+ = 0$, torque balance requires

$$\alpha_p (v_{N-1} - v_N r_0 + r_0 \omega_{N-1} + 3r_0 \omega_N) + \alpha_b r_0 \omega_M = \alpha_b r_0 \omega_0, \quad (\text{A6})$$

which gives Eq. (2) of the main text. Note that we have ignored friction with the outer wall. We additionally assume that ω_i is smooth and continuous at $r = 0$ such that it can be locally expanded as $A + B r_i^2$, for some unknown factors A and B . It follows that

$$(r_2^2 - r_3^2) \omega_1 + r_3^2 \omega_2 - r_2^2 \omega_3 = 0, \quad (\text{A7})$$

which gives the boundary condition at the center of the chamber.

Particles in the i th lane are accelerated by the particles in neighboring lanes and slowed by friction with the bottom surface. The interior lane exerts a tangential force on the i th lane of

$$F_- = m \beta_p [(v_{i-1} + \omega_{i-1} r_0) - (v_i - \omega_i r_0)], \quad (\text{A8})$$

where β_p is a rate coefficient and m is the mass of a particle. Similarly, the exterior lane exerts a force

$$F_+ = m \beta_p [(v_{i+1} - \omega_{i+1} r_0) - (v_i + \omega_i r_0)]. \quad (\text{A9})$$



FIG. 9. The measured velocity profile for the various area fractions ranging from dilute gas to dense crystal and corresponding fits to the coarse-grained model.

The drag on the i th lane is

$$F_D = -m\beta_b v_i. \quad (\text{A10})$$

At steady state, the total torque on each lane is $r_i(F_+ + F_- + F_D) = 0$. Thus,

$$\beta_p(v_{i-1} - 2v_i + v_{i+1} + \omega_{i-1}r_0 - \omega_{i+1}r_0) - \beta_b v_i = 0. \quad (\text{A11})$$

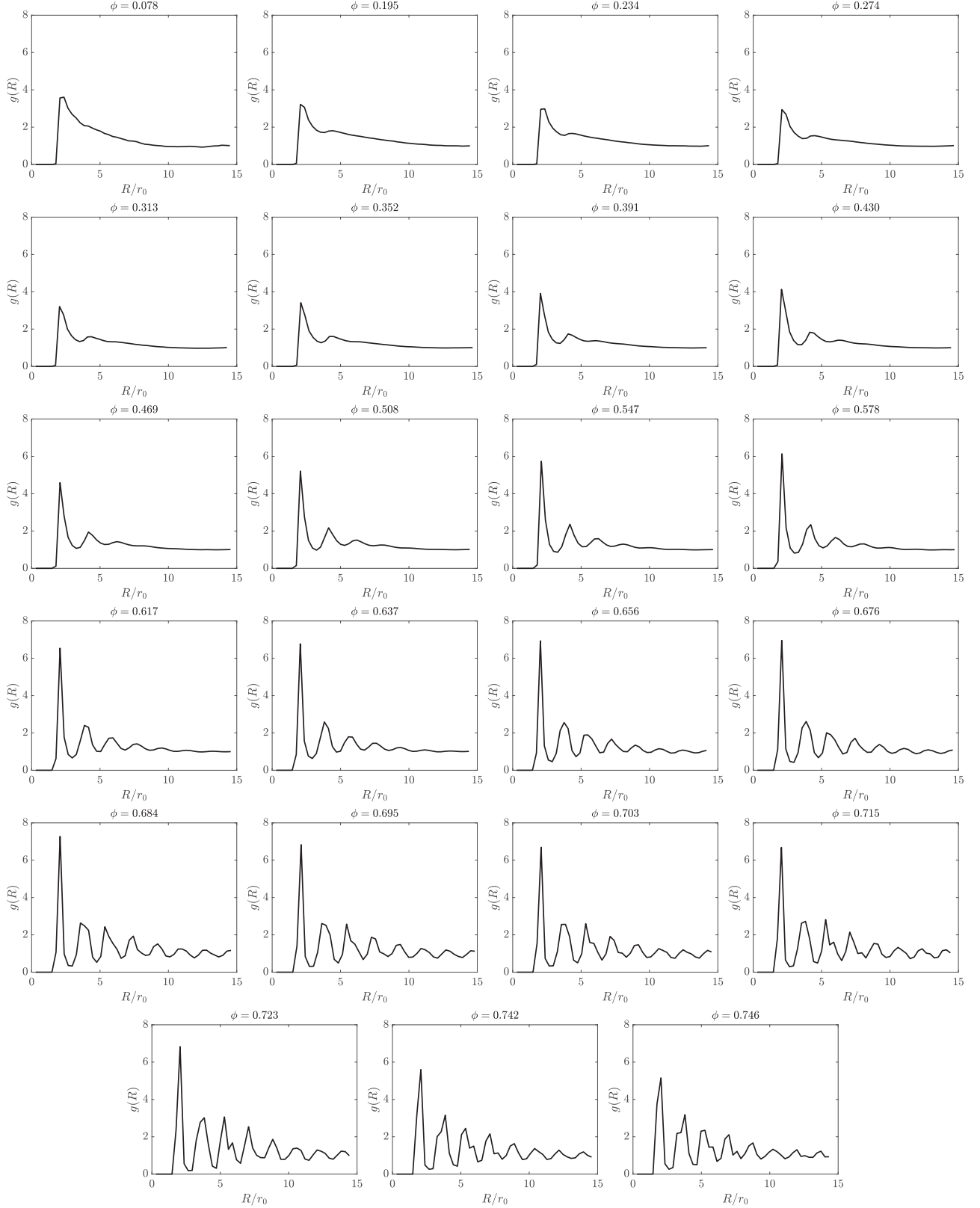


FIG. 10. The measured pair correlation function for the various area fractions ranging from dilute gas to dense crystal.

Nondimensionalizing velocity by $\omega_0 r_0$ and angular velocity by ω_0 yields Eq. (3) of the main text. Particles in the outermost lane only interact with the interior lane. The corresponding torque balance, which requires $\tau_N = r_N(F_- + F_D)$, yields

Eq. (4) of the main text. Again, we assume that Ω is smooth and continuous at the center, implying

$$(r_2^2 - r_3^2)\Omega_1 + r_3^2\Omega_2 - r_2^2\Omega_3 = 0. \quad (\text{A12})$$

Thus, torque balance on each particle [Eqs. (1) and (2) in the main text] and lane [Eqs. (3) and (4) in the main text] along with continuity of particle motion at the center [Eqs. (A7) and (A12)] define $2N$ linear equations for a system composed of N lanes. These equations can be trivially rewritten as

$$\mathbf{M} \begin{pmatrix} \mathbf{v} \\ \boldsymbol{\omega} \end{pmatrix} = \begin{pmatrix} \mathbf{0} \\ \mathbf{1} \end{pmatrix}, \quad (\text{A13})$$

where \mathbf{M} is a matrix composed of elements that vary with α and β , \mathbf{v} is vector with elements v_i , and $\boldsymbol{\omega}$ is vector with elements ω_i . For given values of α and β , we invert \mathbf{M} to find the speed and angular velocity of particles in each lane.

This model is fit to the measured velocity profile by least squares. We provide the fits of the velocity profile for each experiment in Fig. 9. The fitting constants α and β are plotted in Fig. 6 in the main text. Excellent agreement is observed over the entire range of ϕ .

APPENDIX B: FORMATION OF A SPANNING CONTACT NETWORK

We find the contact network in each frame of the experiment from the observed particle locations. Two particles are in contact if their centers are within 10% of a particle diameter. We then identify disjoint clusters (collections of particles in the same contact network). At small area fractions, most clusters contain fewer than three particles. At the highest area fraction, a single cluster is observed. We take a cluster to be spanning if the furthest distance separating the constituent particles is greater than $3R_c/4$. Figure 8(a) shows the weight P of spanning clusters as the fraction of particles in a spanning cluster. We also measure and plot the variance of the sizes of nonspanning clusters N_c in Fig. 8(b). Averaging these

measurements over the length of the experiment, we find that cluster sizes are most widely distributed at an area fraction of $\phi_{\text{perc}} \approx 0.5$. The precise value at which spanning clusters form is sensitive to parameter choices; however, the reported value for the percolation transition is in accord with visual inspection.

APPENDIX C: SUPPLEMENTAL VIDEOS

Three videos of the motion of particles are provided in the Supplemental Material [23].

(1) Video SV1.mp4 shows three representative experiments at three different area fractions, corresponding to the panels of Fig. 1 of the main text.

(2) SV2.mp4 shows the solid-body motion of a crystal composed of 185 particles ($\phi = 0.723$). The image is rotated with the instantaneous angular velocity of the crystal. The contact network is shown with thin black lines. The thick black line shows the orientation of each particle in the rotating frame. Note that particle orientation changes only slightly over the course of the experiment, indicating that particles rotate at a similar speed of the crystal. Many defects in the lattice are apparent. A system scale dislocation, which appears halfway through the video, is highlighted with a red dashed line.

(3) SV3.mp4 shows that, at the highest packing fraction (191 particles, $\phi = 0.746$), particle spin is in phase with the solid-body rotation of the crystalline packing. The thick black lines show the orientation of the particles in the rotating frame. Note that most particles appear stationary in the rotating reference frame, which indicates they spin with the surrounding lattice. A few particles close to lattice defects rotate quickly.

-
- [1] J.-C. Tsai, Fangfu Ye, Juan Rodriguez, J. P. Gollub, and T. C. Lubensky, A Chiral Granular Gas, *Phys. Rev. Lett.* **94**, 214301 (2005).
 - [2] A. P. Petroff, X.-L. Wu, and A. Libchaber, Fast-Moving Bacteria Self-Organize Into Active Two-Dimensional Crystals of Rotating Cells, *Phys. Rev. Lett.* **114**, 158102 (2015).
 - [3] B. C. van Zuiden, J. Paulose, W. T. M. Irvine, D. Bartolo, and V. Vitelli, Spatiotemporal order and emergent edge currents in active spinner materials, *Proc. Natl. Acad. Sci. U.S.A.* **113**, 12919 (2016).
 - [4] K. Dasbiswas, K. K. Mandadapu, and S. Vaikuntanathan, Topological localization in out-of-equilibrium dissipative systems, *Proc. Natl. Acad. Sci. U.S.A.* **115**, E9031 (2018).
 - [5] B. Liebchen and D. Levis, Chiral active matter, *Europhys. Lett.* **139**, 67001 (2022).
 - [6] T. H. Tan, A. Mietke, J. Li, Y. Chen, H. Higinbotham, P. J. Foster, S. Gokhale, J. Dunkel, and N. Fakhri, Odd dynamics of living chiral crystals, *Nature (London)* **607**, 287 (2022).
 - [7] D. Banerjee, A. Souslov, A. G. Abanov, and V. Vitelli, Odd viscosity in chiral active fluids, *Nat. Commun.* **8**, 1573 (2017).
 - [8] C. Scheibner, A. Souslov, D. Banerjee, P. Surówka, W. T. M. Irvine, and V. Vitelli, Odd elasticity, *Nat. Phys.* **16**, 475 (2020).
 - [9] E. S. Bililign, F. B. Usabiaga, Y. A. Ganan, A. Poncet, V. Soni, S. Magkiriadou, M. J. Shelley, D. Bartolo, and W. T. Irvine, Motile dislocations knead odd crystals into whorls, *Nat. Phys.* **18**, 212 (2022).
 - [10] G. Kokot, S. Das, R. Winkler, G. Gompper, I. Aranson, and A. Snezhko, Active turbulence in a gas of self-assembled spinners, *Proc. Natl. Acad. Sci. USA* **114**, 12870 (2017).
 - [11] K. Drescher, K. C. Leptos, I. Tuval, T. Ishikawa, T. J. Pedley, and R. E. Goldstein, Dancing Volvox: Hydrodynamic Bound States of Swimming Algae, *Phys. Rev. Lett.* **102**, 168101 (2009).
 - [12] A. P. Petroff and A. Libchaber, Nucleation of rotating crystals by *Thiovulum majus* bacteria, *New J. Phys.* **20**, 015007 (2018).
 - [13] C. Reichhardt and C. J. O. Reichhardt, Dynamics and nonmonotonic drag for individually driven skyrmions, *Phys. Rev. B* **104**, 064441 (2021).
 - [14] M. Brandenbourger, C. Scheibner, J. Veenstra, V. Vitelli, and C. Coulais, Limit cycles turn active matter into robots (2021).
 - [15] C. Scholz, A. Ldov, T. Pöschel, M. Engel, and H. Löwen, Surfactants and rotelles in active chiral fluids, *Sci. Adv.* **7**, eabf8998 (2021).
 - [16] D. L. Blair, T. Neicu, and A. Kudrolli, Vortices in vibrated granular rods, *Phys. Rev. E* **67**, 031303 (2003).

- [17] E. Altshuler, J. M. Pastor, A. Garcimartín, I. Zuriguel, and D. Maza, Vibrot, a simple device for the conversion of vibration into rotation mediated by friction: Preliminary evaluation, *PLoS ONE* **8**, e67838 (2013).
- [18] N. Koumakis, A. Gnoli, C. Maggi, A. Puglisi, and R. Di Leonardo, Mechanism of self-propulsion in 3d-printed active granular particles, *New J. Phys.* **18**, 113046 (2016).
- [19] C. Scholz, M. Engel, and T. Pöschel, Rotating robots move collectively and self-organize, *Nat. Commun.* **9**, 931 (2018).
- [20] M. A. López-Castaño, A. Rodríguez-Rivas, and F. Vega Reyes, Chiral flow in a binary mixture of two-dimensional active disks, *Front. Phys.* **10**, 972051 (2022).
- [21] P. Liu, H. Zhu, Y. Zeng, G. Du, L. Ning, D. Wang, K. Chen, Y. Lu, N. Zheng, F. Ye, and M. Yang, Oscillating collective motion of active rotors in confinement, *Proc. Natl. Acad. Sci. USA* **117**, 11901 (2020).
- [22] D. Volfson, A. Kudrolli, and L. S. Tsimring, Anisotropy-driven dynamics in vibrated granular rods, *Phys. Rev. E* **70**, 051312 (2004).
- [23] See Supplemental Material at <http://link.aps.org/supplemental/10.1103/PhysRevE.108.014609> for movies of representative experiments.
- [24] M. Workamp, G. Ramirez, K. E. Daniels, and J. A. Dijksman, Symmetry-reversals in chiral active matter, *Soft Matter* **14**, 5572 (2018).
- [25] V. Soni, E. S. Bililign, S. Magkiriadou, S. Sacanna, D. Bartolo, M. J. Shelley, and W. Irvine, The odd free surface flows of a colloidal chiral fluid, *Nat. Phys.* **15**, 1188 (2019).
- [26] X. Yang, C. Ren, K. Cheng, and H. P. Zhang, Robust boundary flow in chiral active fluid, *Phys. Rev. E* **101**, 022603 (2020).
- [27] P. M. Reis, R. A. Ingale, and M. D. Shattuck, Caging Dynamics in a Granular Fluid, *Phys. Rev. Lett.* **98**, 188301 (2007).